Acta Pharmaceutica Sinica B 2026;16(7):4725−4738

Chinese Pharmaceutical Association
Institute of Materia Medica, Chinese Academy of Medical Sciences

Acta Pharmaceutica Sinica B

www.elsevier.com/locate/apsb
www.sciencedirect.com

ORIGINAL ARTICLE

Dual-pathway induction of pyroptosis *via* biomineralized-like nanoparticles trigger potent immunotherapy against tumor

Jiaxing Feng[a], Kun Xiong[a], Yuan Xue[a], Yating Wang[a], Xiuhua Wu[b], Qing Lin[a], Xun Sun[a], Huile Gao[a], Zhirong Zhang[a], Tao Gong[a,*]

[a]*Key Laboratory of Drug-Targeting and Drug Delivery System of the Education Ministry & Sichuan Engineering Laboratory for Plant-Sourced Drug and Sichuan Research Center for Drug Precision Industrial Technology, West China School of Pharmacy, Sichuan University, Chengdu 610041, China*
[b]*NMPA Key Laboratory for Technical Research on Drug Products In Vitro and In Vivo Correlation, Sichuan Institute for Drug Control, Chengdu 611731, China*

Received 12 August 2025; received in revised form 17 January 2026; accepted 24 January 2026

KEY WORDS

Cancer immunotherapy;
Pyroptosis;
Starvation therapy;
DNA demethylation;
Immune checkpoint inhibitor

Abstract Pyroptosis, a highly pro-inflammatory form of immunogenic cell death, holds great promise for cancer treatment. However, its efficacy in cancer cells is often limited due to low efficiency and cellular complex pro-survival mechanisms. In this study, we address this challenge by an integrated nanoplatform simultaneously activating two pathways of pyroptosis. Manganese ions and imidazole serve as a framework to coordinate glucose oxidase (GOx) and epigallocatechin gallate (EGCG) into stable biomineralized-like nanoparticles. We hypothesize that EGCG, as an inhibitor of DNA methyltransferase, may restore the expression of Gasdermin E (GSDME), a crucial component of pyroptosis activated by cleaved caspase-3. Through glucose consumption, GOx triggers both the caspase-1/Gasdermin D (GSDMD)-mediated and caspase-3/GSDME-mediated pathways of pyroptosis simultaneously, leading to efficient pyroptosis in cancer cells and a robust anti-tumor immune response, accompanied by the up-regulated expression of PD-L1. Our results reveal that integrating this strategy with immune checkpoint inhibitors results in a tumor inhibition rate exceeding 80% across several "cold" tumor models, a 20% cure rate in the CT26 unilateral tumor model, and 5/8 distant tumors remaining free of recurrence upon re-challenge. In conclusion, this dual-pathway induction of pyroptosis offers a novel and promising strategy for enhancing cancer immunotherapy.

*Corresponding author.
E-mail address: gongtaoy@126.com (Tao Gong).

Peer review under the responsibility of Chinese Pharmaceutical Association and Institute of Materia Medica, Chinese Academy of Medical Sciences.

https://doi.org/10.1016/j.apsb.2026.01.034

1. Introduction

Pyroptosis, as a pro-inflammatory immunogenic cell death (ICD), shows great potential for anti-tumor therapy[1-4]. Pyroptosis is mainly caused by activated cysteine proteases (caspase 1/3/4/5/8/11 and so on) that cleave "Gasdermin" family proteins (including GSDM A-E and DFNB59), the N-terminal of which is located on the cell membrane to form pores[2,5,6]. Then, these nanoscale pores cause cell swelling and blowing, as well as a large amount of contents, including tumor-associated antigens (TAAs) and pro-inflammatory cytokines and so on, to be released from inside to outside the cells, followed by the initiation of anti-tumor immune responses[7,8]. Besides, pyroptosis is reported to be accompanied by upregulation of PD-L1[9-11]. Therefore, the combination of pyroptosis and immune checkpoint inhibitors (ICIs) may have a synergistic effect to achieve a long-lasting and powerful effect against tumors[11-16].

Specifically, the caspase-1/GSDMD, a canonical pyroptosis signaling pathway, is always activated by cellular stress, such as reactive oxygen species (ROS), glucose starvation and so on. For example, the agent for tumor starvation therapy, glucose oxidase (GOx), has been reported to activate the caspase-1/GSDMD mediated pyroptosis by regulating glucose metabolism in tumor cells[17-19]. In this process, the depletion of glucose and oxygen and the accumulation of ROS also act as internal stimuli to induce caspase 3-mediated apoptosis, which may cause tumor cells to be more tolerant to death and the tumor microenvironment (TME) to be more deeply immunosuppressed, due to the low levels of damage-associated molecular patterns (DAMPs) and efferocytosis of tumor-associated macrophages (TAMs)[20-22]. Therefore, the limited induction efficiency of a single pyroptosis pathway, the immunosuppressive tumor microenvironment (TME) and the existence of multiple complex pro-survival mechanisms within tumor cells may all restrict the effectiveness of pyroptosis in practical applications.

Another deeply-studied effector molecule, GSDME, is regarded as a tumor suppressor, due to the fact that its expression in most tumor cells is downregulated by the high methylation of the DFNA5 gene[4,23,24]. Epigenetic strategies are considered to be one of the important approaches to DNA demethylation in clinic[4,25,26]. In addition to its properties of adhesion, high biocompatibility and apoptosis induction in tumor cells, EGCG is also used as a DNA methyltransferase inhibitor[27-29]. In this study, we verified the universality of its demethylation to DFNA5 gene in mouse and human tumor cells and then speculated that the combination of EGCG can convert caspase-3 mediated apoptosis to caspase-3/GSDME mediated pyroptosis, which is expected to avoid tolerance mechanisms and achieve a strong anti-tumor effect through efficient pyroptosis of cancer cells[4,15,23,24].

Here, this study proposed a new strategy based on pyroptosis, which was simultaneously activated by the signaling pathways mediated by caspase 1-GSDMD and caspase 3-GSDME, inducing efficient pyroptosis with low-dose drugs, releasing enough TAAs and inflammatory cytokines, and reversing the immunosuppressive TME. Further combined with PD-L1 antibodies, a powerful anti-tumor immunotherapy would be achieved. Inspired by natural biomineralization and metal organic frameworks, this work used a one-pot approach to chelate GOx and EGCG based on the framework composed of manganese ions and 2-methylimidazole to construct nanoparticles named GME NPs[30,31]. This preparation method with simple procedures achieved the effective loading of two hydrophilic drugs; in addition, the presence of EGCG also participates in the construction of nanoparticles, further improving the stability of the nanoparticles. After being taken up, in the acidic environment of lysosomes, GME NPs were dissociated and released the active ingredients of GOx and EGCG, due to the destruction of the coordination effect. EGCG, as an inhibitor of the DNA methyltransferase, would restore or upregulate the expression of GSDME in tumor cells. Then GOx activated the caspase 1-GSDMD mediated pyroptosis through the consumption of glucose, accompanied by upregulation of PD-L1. At the same time, the consumption of intracellular glucose and the increase of oxidative stress would also promote the cleavage of caspase 3 and apoptosis, but the upregulated expression of GSDME would convert this apoptosis into pyroptosis. In general, through this ingenious integrated nanoplatform, the dual activation of caspase 1-GSDMD and caspase 3-GSDME signal pathways could greatly improve the efficiency of pyroptosis, which was accompanied by the release of a large amount of pro-inflammatory intracellular contents, the improved tumor immunogenicity, and the remodeled TME. Combined with PD-L1 immunotherapy agents, great anti-tumor efficacy has been achieved in multiple tumor models. Besides, the reduction of the required GOx dose could also effectively avoid the side effects, such as hypoglycemia caused by GOx entering the blood, and excessive inflammation and tissue damage caused by caspase-1 mediated pyroptosis.

2. Materials and methods

2.1. GSDME expression in tumor cells upregulated by EGCG

CT26 and HT29 cells in the logarithmic growth phase were seeded on 24-well plates at a density of 3×10^4 cells per well. Overnight, the medium was replaced with 0.5 mL of medium or medium containing DAC (1 or 5 μmol/L) or EGCG (1, 2, 5, or 10 μmol/L) and cells were incubated for another 24 h for RT-qPCR assays and WB analysis.

2.1.1. Bisulfite sequencing PCR (BSP) assays

CT26 and HT29 cells, with or without EGCG treatment, were harvested and washed with PBS. Genomic DNA was then extracted using a commercial DNA extraction kit, quality was confirmed by MicroDrop analysis. DNA samples were then subjected to bisulfite conversion using a DNA methylation−bisulfite conversion kit. BSP primers were designed based on highly methylated regions within the DFNA5 promoter of CT26 and HT29, shown in Supporting Information Table S1. PCR amplification was performed, specificity verified by gel electrophoresis, followed by cloning, sequencing, and methylation analysis.

2.1.2. RT-qPCR assays

After being washed by PBS, the total RNA of cells was extracted and purified through the manufacturer's instructions. And the concentration and the purity of RNA were detected by Nano-Drop. Subsequently, the reverse transcription of total RNA was conducted. Then, the cDNA obtained by reverse transcription was amplified and detected by real-time PCR. Finally, the relative expression level of the mRNA of GSDME was calculated by the internal reference gene GAPDH. The base sequences of the primers are shown in Supporting Information Table S2.

2.1.3. WB analysis

The treated cells were collected, washed with PBS and lysed on ice for 30 min. The extracted proteins were quantified using BCA assay kit. After normalization, the proteins were separated by a 10% SDS-PAGE gel and subsequently transferred to a 0.22 μm PVDF membrane. The PVDF membrane was incubated with TBST containing skim milk for 1 h at RT, the primary antibody at 4 °C overnight, and the secondary antibody for 1 h at RT, in turn. Finally, the ECL solution was dropped on the PVDF membrane, and the chemiluminescence was detected using the gel imaging technique to visualize the proteins. Semi-quantitative analysis of the proteins was performed using ImageJ software.

2.2. Preparation of GME and GMN NPs

GOx, EGCG, 2-methylimidazole and Mn^{2+} were dissolved in sterile water respectively, and then added together under stirring. Stirring was continued at room temperature (RT) for 1 h. The reaction solution was centrifuged (12,000 rpm, 30 min) and washed with sterile water for 2−3 times. Finally, GME NPs were obtained by re-suspending.

Similarly, GOx, 2-methylimidazole and Mn^{2+} were dissolved in sterile water respectively, and then added together under stirring. Stirring was continued at RT for 1 h. The reaction solution was centrifuged (12,000 rpm, 30 min) and washed with sterile water for 2−3 times. Finally, GMN NPs were dispersed by probe ultrasonication (150 w, 10 min).

2.3. Study on the anti-tumor efficacy of GME NPs

2.3.1. The establishment of tumor model

To establish the model of CT26 subcutaneous tumor-bearing mice, 1×10^6 CT26 cells in the logarithmic growth phase were re-suspended in 100 μL sterile PBS, and then subcutaneously injected into the right back of female BALB/c nude mice (6−8 weeks old, 18−22 g). It was worth mentioning that female BALB/c nude mice were chosen here to avoid interference caused by hair or others, so as to observe the intratumor retention more clearly.

2.3.2. Anti-CT26 unilateral subcutaneous tumor

To establish the model of CT26 subcutaneous tumor-bearing mice, 1×10^6 CT26 cells in the logarithmic growth phase were re-suspended in 100 μL sterile PBS, and then subcutaneously injected into the right back of female BALB/c mice (6−8 weeks old, 18−22 g). After being inoculated for 8 days, the average of tumor volume reached about 75 mm^3. Then, the tumor-bearing mice were randomly divided into six groups ($n = 15$), namely Saline, GOx, αPD-L1, GMN, GME and GME+αPD-L1 (the dosage of GOx: 25 μg/mouse). On the 8th and 12th days, different preparations were injected intratumorally, and then αPD-L1 was injected intraperitoneally about 24 h after intratumoral injection (the dosage of αPD-L1: 100 μg/mouse). The body weight and tumor volume were recorded every other day, and the latter was calculated as Eq. (1):

$$\text{Tumor volume} = \frac{\text{Length} \times \text{width} \times \text{width}}{2} \quad (1)$$

Five days after the last treatment, 5 of tumor-bearing mice from each group were taken sacrificed. And then the CT26 tumors were excised, imaged, and weighed, and the tumor growth inhibition (TGI) was calculated by the following formula. The excised tumors were fixed in 4% paraformaldehyde for histological examination, immunohistochemical (IHC) and immunofluorescence (IF) staining, including conventional H&E, TUNEL, Ki67 antigen staining, as well as CRT and HMGB1 represented as ICD, and cleaved caspase 1 and cleaved caspase 3 represented as pyroptosis. The remaining 10 mice of each group were used for the survival study, and Kaplan−Meier curves were used for the analysis of the survival. It should be noted that except for the death due to non-environmental causes, the tumor volume of tumors over 2000 mm^3 or the length of tumors over 20 mm was also considered sacrificial.

$$\text{TGI}\,(\%) = 1 - \frac{\text{Weight of tumors after different treatment}}{\text{Weight of tumors treated with Saline}} \times 100 \quad (2)$$

2.3.3. Anti-CT26 re-challenge tumor

The inhibitory effect on distant tumors caused by the immune response of GME NPs was further investigated. Firstly, as described above, unilateral CT26 subcutaneous tumor model was established, and three treatment cycles were performed. Five days after the last administration, 2×10^6 of CT26 cells were subcutaneously inoculated on the left side of tumor-bearing mice. Since most of the tumor-bearing mice in the saline group were sacrificed already, the saline group of distant tumors was established on the healthy mice. The volume of primary tumors and distant tumors was recorded and calculated as described above.

3. Results and discussion

3.1. The fabrication and characterization of biomineralized-like GME NPs

The preparation process and schematic diagram of GME NPs were shown in Fig. 1A. The particle size and zeta potential of the GME NPs were about 134.6 nm and −20.1 mV, respectively (Fig. 1B and Supporting Information Table S3 and Fig. S1D). In addition, the GME NPs were nearly spherical with a particle size of approximately 75 nm in the vacuum-dried state, which was visually observed by transmission electron microscopy (TEM; Fig. 1B and Fig. S1A). Based on the principle of enzymatic reaction, the encapsulation efficiency (EE) and drug loading (DLC) of GOx in GME were calculated to be 43.8 ± 5.4% and 24.3 ± 3.1%, respectively (Table S3). The preparation method of the control nanoparticles called GMN NPs was referred to in the reported work, and characterized (Table S3 and Fig. S1B−S1D). Additionally, the content of Mn^{2+} loaded in GMN or GME NPs were measured by ICP-OES (Table S3). Furthermore, the activity of GOx loaded in GME NPs was also well maintained, remaining above 90% within 15 days (Fig. 1C).

As shown in Fig. 1D, the particle size of GME NPs did not change a lot within 15 days, while GMN NPs quickly aggregated

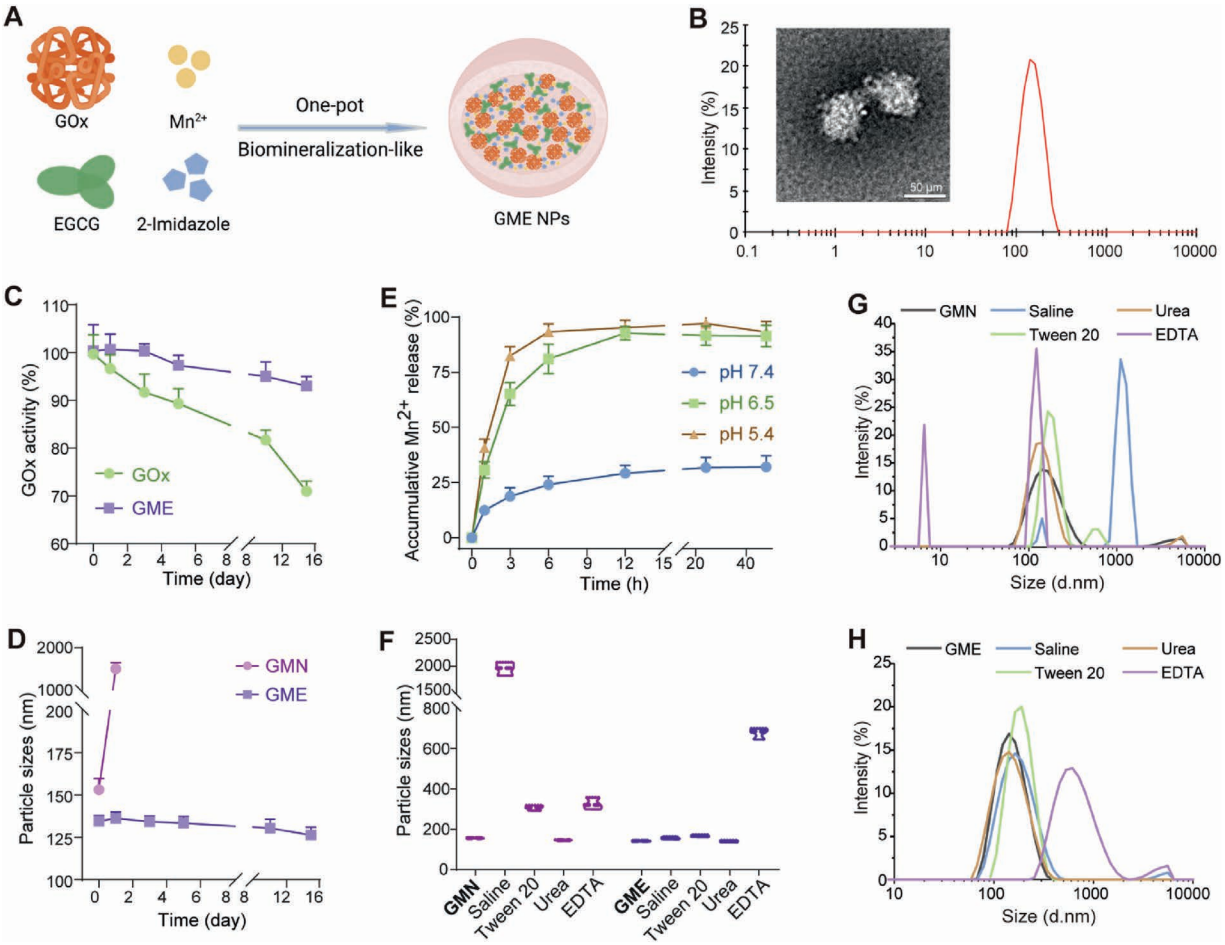

Figure 1 Fabrication and characterization of GME NPs. (A) Schematic illustration of the fabrication of GME NPs. (B) Particle size distribution and representative TEM image of GME NPs. (C) Changes in the enzyme activity of GOx in the free form or encapsulated in GME NPs. (D) Storage stability was evaluated by the changes in particle sizes. (E) Release profile of Mn^{2+} from GME NPs in HEPES buffer (pH 7.4, 6.5, or 5.4) as measured by ICP-OES. (F) Changes in particle sizes of GMN NPs (G) or GME NPs (H) after being incubated with saline, Tween 20, urea, or EDTA for 24 h. Data are shown as mean ± SD ($n = 3$).

and precipitated within 12 h, suggesting that the addition of EGCG significantly improved the stability of GME NPs, which may be due to changes in the surface charge of the nanoparticles and its interactions with other components.

To elucidate formation mechanisms of GME and GMN NPs, their structural interactions were investigated through coordination competition experiments and FTIR analysis (Fig. 1F–H and Fig. S1I)[32,33]. The formation of GME NPs was found to be primarily driven by coordination interactions between Mn^{2+} and the functional groups of GOx, imidazole, and EGCG, with only minor contributions from hydrophobic forces (Fig. 1F–H). In contrast, the formation of GMN NPs was disrupted by a broader range of competing agents (Fig. 1F and G), suggesting the involvement of multiple intermolecular forces. Moreover, various combinations of the core components (GOx, imidazole, EGCG, Mn^{2+}) was mixed systematically to monitor the appearance of the Tyndall effect, also indicating the existence of every component and their importance for the formation of GME NPs (Fig. S1J).

To further support these findings, FTIR spectra were performed on free GOx, imidazole, GMN NPs, and GME NPs (Fig. S1I). The C=N stretching vibration peak of imidazole at 1593 cm^{-1} exhibited blue-shifted in GMN NPs, suggesting coordination between imidazole and Mn^{2+} [34-36]. In GME NPs, this peak was further broadened, indicating that the added EGCG also interacted with the C=N and confirming the incorporation of EGCG. The carboxyl stretching vibration peak of GOx at 1395 cm^{-1} shifted to lower wavenumbers and exhibited peak splitting in GMN NPs, suggesting an interaction between GOx and Mn^{2+} [37,38]. In addition, in GME NPs, the broadening and increased intensity of this peak imply enhanced interactions, possibly due to the interactions between EGCG and other components, further stabilizing the nanoparticles structure.

Nanoparticles composed of metal-imidazole or metal-phenolic frameworks were always formed by coordination effects and were easily dissociated under acidic conditions. Not surprisingly, GME NPs also displayed the pH-dependent release behavior in HEPES buffer (Fig. 1E). The cumulative release of Mn^{2+} reached nearly 100% within 6 h at pH 5.4 and 12 h at pH 6.5, while remaining at ~24% at pH 7.4 after 48 h, confirming the acid-sensitive disassembly profile of the nanoparticles. To simulate the degradation of GME NPs in the tumor microenvironment *in vitro*, this assay was repeated in PBS (Fig. S1E). GME NPs were affected by the reactions between phosphate and manganese ion, exhibiting faster degradation and release.

Moreover, the catalytic effect *in vitro* of different forms of GOx was investigated by changes in glucose concentration, pH of the solution, and production of H_2O_2 (Fig. S1F−S1H). The results showed that GOx, GMN NPs and GME NPs could specifically consume glucose and generate glucuronic acid to lower the pH of the solution. Meanwhile, the addition of Mn^{2+} loaded in the GMN and GME NPs notably reduced the accumulation of H_2O_2 generated by reaction of GOx and glucose, compared to the free GOx group, which might be beneficial to the positive cycle of glucose consumption. At the beginning, since GOx in GMN NPs and GME NPs was encapsulated inside the nanoparticles, their catalytic rates were slightly slower than that of free GOx. However, companied by the decreased pH and the existence of Mn^{2+}, the nanoparticles were gradually degraded and their catalytic rates also tended to be consistent.

3.2. GME NPs induced pyroptosis by the dual-activation of caspase 1-GSDMD and caspase 3-GSDME

Numerous studies have reported that reduced DFNA5 expression in tumor cells is mainly due to hypermethylation of its promoter region[4,24,39]. As hypothesized, BSP analysis revealed that EGCG treatment induced varying degrees of demethylation in the DFNA5 promoter region of both CT26 and HT29 cells (Supporting Information Figs. S2A and S3A). These genomic-level results directly support EGCG's demethylation effect.

Furthermore, consistent with BSP findings, mRNA levels of DFNA5 were significantly increased after EGCG treatment, and GSDME protein levels were correspondingly upregulated, providing coherent transcriptional and translational evidence aligned with the promoter demethylation results (Fig. 2A). RT-qPCR data showed that EGCG could effectively restore or upregulate the transcription of the DFNA5 gene in CT26 (Fig. 2B). After 24 h of EGCG (2 μmol/L) treatment, the transcription level of GSDME in CT26 was 2.50 times that of the negative control group. However, the transcription level of GSDME decreased after treatment with a higher concentration of EGCG (10 μmol/L), which might be due to cell stress caused by the cytotoxicity of EGCG (Fig. S2C)[40,41]. It is worth noticing that during this experiment, bubbles were indeed observed in tumor cells treated with EGCG (25 μmol/L or higher), which showed concentration-dependent characteristics (Fig. S2D)[1,3,4]. This also indirectly suggested that EGCG at a low concentration could restore the expression of GSDME, and then effectively improve the proportion of pyroptosis in cell death, as the concentration of EGCG increased. The WB results showed that the expression level of GSDME-FL basically upregulated, as the concentration of EGCG increased (Fig. 2C and Fig. S2B). Even if the mRNA expression level of GSDME decreased at 5 μmol/L EGCG concentration, the GSDME-FL was still increased in the WB analysis, which might be due to the stability of the already synthesized protein and its continuous accumulation. Similar phenomena were also observed in HT29 (Fig. S3). In general, it was verified that EGCG could significantly increase the expression of GSDME *via* DNA demethylation.

The mean fluorescence intensity (MFI) of uptake of GME NPs on CT26 was 3.11 and 1.95 times that of GOx and GMN NPs, respectively (Fig. 2D). And the cytotoxicity of GME NPs on CT26 was similar to free GOx and significantly stronger than that of GMN NPs (Fig. 2E and Supporting Information Table S4). Similar results were also shown in 4T1 (Supporting Information Fig. S6A and S6B). We speculated this potent cytotoxicity of free GOx may result from its extracellular enzymatic effects rather than intracellular pathway activation. Free GOx is a ∼150 kDa, highly hydrophilic, negatively charged protein under physiological conditions. Such macromolecules cannot diffuse through the phospholipid bilayer, and typically consume glucose and accumulate H_2O_2 outside the cells, resulting cytotoxicity. We also conducted additional glucose assays to directly compare glucose levels in the culture medium and cells, confirming that free GOx markedly reduces extracellular glucose, reinforcing its indirect cytotoxicity (Supporting Information Fig. S4H and S4I). However, GME NPs showed significantly enhanced cytotoxicity on HT29 compared with free GOx and GMN NPs (Fig. 3B and Table S4). These results might be attributed to the demethylation effect of EGCG on the DFNA5 gene and the synergistic effect of activation of the caspase 3-GSDME mediated pyroptosis, considering that HT29 was reported to be highly methylated and barely expressed GSDME[4,41].

The occurrence of pyroptosis is usually faster than apoptosis, accompanied by permeabilization of the cell membranes[4,42]. The proportion of Annexin V^+/PI^+ was the highest in CT26 treated with the GME NPs, even twice that of the GOx or GMN NPs group, while the proportion of Annexin V^+/PI^- was similar (Fig. 2F). Similar results were observed in HT29 and 4T1 (Fig. 3C and Fig. S6D). This suggested that the GME NPs induced a faster and more powerful pyroptosis than GOx and GMN NPs, before early apoptosis. Bubbles blowing from cell membranes are regarded as the gold standard to evaluate pyroptosis[1,3,4]. Similar to the cytotoxicity assays, GME NPs and GOx induced extensive bubbles in CT26 or 4T1, followed by GMN NPs (Fig. 2G and Figs. S4A, S6E and S6F). And in HT29, extensive bubbles appeared in cells treated with the GME NPs at two different dosing concentrations, while only a few bubbles were observed in the GOx or GMN NPs group (Fig. 3D and Supporting Information Fig. S5A and S5B). The release of lactate dehydrogenase (LDH) was also reported as one of the typical characteristics of pyroptosis[1,3,23]. The ratio of LDH released to the culture supernatant were also consistent with the cytotoxicity assays (Fig. 2J and Fig. S6C). And in HT29, cells treated with GME NPs exhibited the highest LDH release (Fig. S5E). These phenomena again suggested that pyroptosis induced by the GME NPs were highly efficient, which due to the upregulated expression of GSDME by EGCG and dual-pathway induction of pyroptosis. In order to evaluate the mechanism of GME NPs-induced pyroptosis in tumor cells, the activation of caspase 1 and caspase 3 was characterized by immunofluorescence technology (IF), and Western blot technology (WB) was used to characterize the expression levels of the key effectors called GSDMD and GSDME. The presence of cleaved caspase 1 and GSDMD-N terminal (the active form of GSDMD) was observed in CT26 cells treated with different GOx preparations (Fig. 2H−I and Fig. S4B−S4G). However, cell stress induced by GOx inevitably activated caspase 3, and the specific fluorescence of cleaved caspase 3 was captured in cells treated with different forms of GOx). However, significant upregulation of GSDME and GSDME N-terminal was observed only in the GME NPs group. The same dual-pathway induction of pyroptosis was also declared in HT29 (Fig. 3E−I and Fig. S5C−S5E). These results strongly suggest that after entering the tumor cells, GME NPs were dissociated to release EGCG and GOx. EGCG entered the nucleus to inhibit methyltransferase and restore GSDME expression, while GOx triggered the caspase 1-GSDMD pathway *via* cell stress caused by glucose depletion and H_2O_2 generation, and shifted caspase 3-mediated apoptosis to GSDME-mediated pyroptosis (Fig.

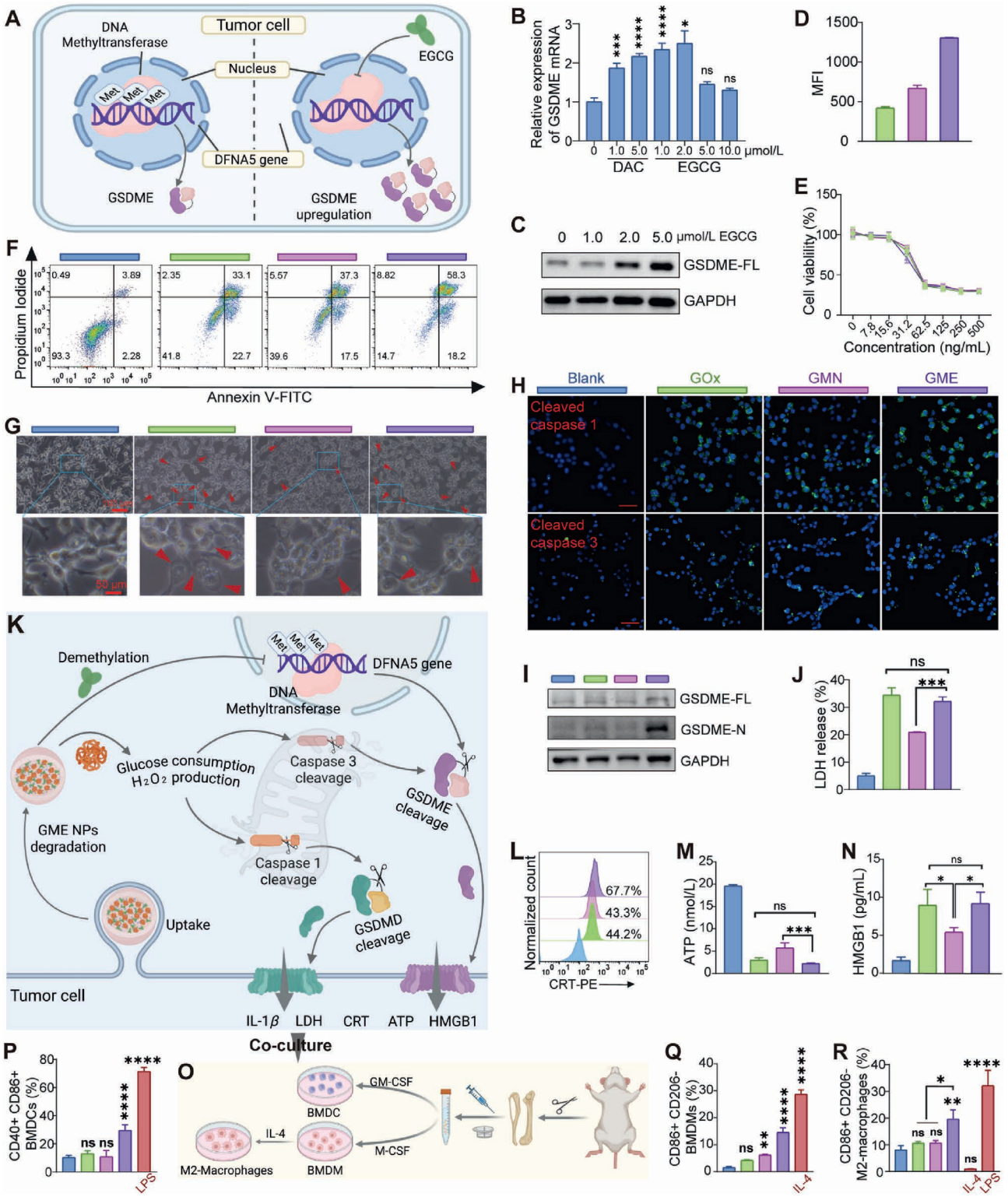

Figure 2 GME NPs induced pyroptosis *via* dual activation of caspase 1-GSDMD and caspase 3-GSDME pathways in CT26 mouse tumor cells. (A) Schematic illustration of EGCG-mediated demethylation in tumor cells. (B, C) RT-qPCR and WB analyses of GSDME expression in CT26 treated with different EGCG concentrations. (D) Cellular uptake. (E) Cytotoxicity assays. (F) Apoptosis analysis. (G) Representative images showing membrane bubble formation. Scale bar = 100 μm. (H) Representative images of IF staining of cleaved caspase 1 and cleaved caspase 3. Scale bar = 50 μm. (I) WB analysis of full-length GSDME and GSDME-N terminal. (J) LDH release assays. (K) Schematic illustration of the intracellular mechanism of GME NPs. (L−N) ICD markers: CRT exposure, ATP release, and HMGB1 secretion. (O) Schematic illustration of BMDC and BMDM extraction and stimulation with tumor cell supernatant. (P) Maturation of BMDCs. (Q, R) Polarization of BMDMs and the repolarization of IL-4-stimulated BMDMs. Data are shown as mean ± SD ($n = 3$). Statistical significance: ns, $P > 0.05$; *$P < 0.05$; **$P < 0.01$; ***$P < 0.001$; ****$P < 0.0001$.

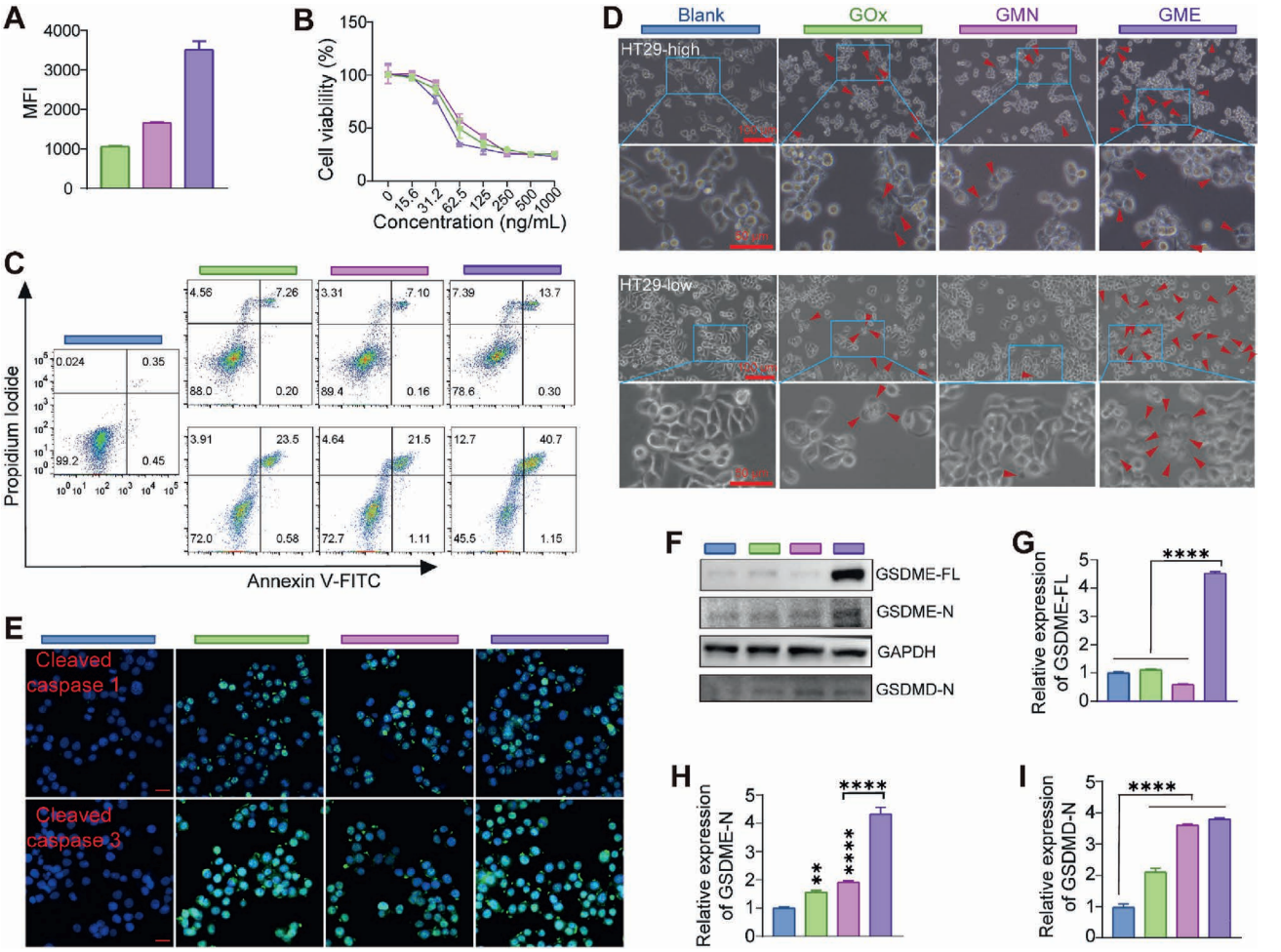

Figure 3 GME NPs induced pyroptosis by the dual-activation of caspase 1-GSDMD and caspase 3-GSDME in human tumor cell line HT29. (A) Cellular uptake. (B) Cytotoxicity assays. (C) Apoptosis analysis, at the GOx concentration of 100 ng/mL for 6 h or 50 ng/mL for 12 h. (D) Bubbles blowing from cytomembrane, at the GOx concentration of 50 ng/mL for 6 h or 50 ng/mL for 12 h. Scale bar = 100 μm. (E) Representative images of IF staining of cleaved caspase 1 or cleaved caspase 3. Scale bar = 20 μm. (F) WB assays and the semi-quantitative analysis of the relative expression GSDME-full length (G), GSDME-N terminal (H) and GSDMD-N terminal (I). Data are shown as mean ± SD ($n = 3$). Statistical significance: ns, $P > 0.05$; *$P < 0.05$; **$P < 0.01$; ***$P < 0.001$; ****$P < 0.0001$.

2K)[43,44]. Therefore, the GME NPs in this study could induce dual-pathway of pyroptosis and achieve the potent immune response against tumor *in vivo*.

Besides, pyroptosis, as a potent ICD, is often accompanied by the exposure of calreticulin (CRT) from the endoplasmic reticulum to the cytomembrane, and the intracellular ATP and high mobility group box-1 protein (HMGB1) in the nucleus are released to the extracellular space through pore-forming proteins[1,45]. CT26 cells treated with the GME NPs showed the highest ratio of positive CRT, the lowest content of ATP in the intracellular space, and the most released HMGB1 in the culture supernatant (Fig. 2L−N). In HT29 and 4T1, similar results were shown (Fig. S5F−S5H, S6G and S6H).

Based on the above data, bone marrow-derived dendritic cells (BMDCs), bone marrow-derived macrophages (BMDMs), and IL-4 polarized BMDMs were used to co-culture with tumor cells *in vitro* to preliminarily explore the stimulation on immune cells by pyroptosis of tumor cells induced by GME NPs (Fig. 2O)[46-49]. The activation of T cells depends on the maturation of BMDCs. Compared with the blank group, the supernatant of tumor cells treated with GME NPs could effectively upregulate the expression of CD40 and CD80 on the surface of BMDCs (Fig. S4J). Compared with the blank group, the proportion of CD40/CD86 double-positive cells remained basically unchanged after the stimulation of GOx and GMN NPs, while the proportion of double-positive cells in the GME NPs group reached 29.48%, which was 2.87 times that of the blank group (Fig. 2P). And BMDMs and IL-4 polarized BMDMs were used to investigate the polarization effect on M0-like macrophages and the re-polarization effect on M2-like macrophages of pyroptosis induced by GME NPs. In BMDMs, the proportions of M1-phenotype macrophages represented by CD86 positive cells were significantly increased in the GOx, GMN NPs and GME NPs groups, which were 2.64, 3.88 and 9.09 times that of the blank group, respectively (Fig. 2Q). In IL-4 polarized BMDMs, the significantly increased proportion of CD86 positive cells was only found in the GME NPs group, and the proportions of M2-phenotype macrophages represented by CD206 positive cells

were observed to decrease in the GOx, GMN NPs and GME NPs groups, which were 86.22%, 82.09%, and 54.48% of the blank group, respectively (Fig. S4K). These above results indicated that GME NPs could effectively stimulate the maturation of BMDCs and promote the polarization of macrophages to the M1-phenotype with the anti-tumor effects *in vitro*, which would be beneficial to initiate and support anti-tumor immune responses.

3.3. GME NPs with an extended retention at tumors exhibited excellent tumor growth inhibition in varied tumors combined with PD-L1 antibody

As a polyphenol compound, one of the characteristics of EGCG is strong adhesion[50]. It is speculated that GME NPs may form a "drug bank" at tumors after intratumoral administration to avoid possible side effects, such as hypoglycemia, and decrease the number of administrations. Therefore, we used the *in vivo* imaging system (IVIS) to investigate the retention of Cy5-labeled GME NPs at tumors. The representative intratumoral fluorescence intensity images were shown in Fig. 4A. The intratumoral fluorescence was further semi-quantitatively analyzed (Supporting Information Fig. S7). Subsequently, the intratumoral fluorescence intensity of tumors at 1 h was used as a reference, and the fluorescence intensity at different time points was normalized (Fig. 4B). The intratumoral fluorescence of the GOx-Cy5 group decreased rapidly after injection, which might be carried away by the fluid at the tumors. There were about 50% of fluorescence intensity at 1 h that could still be detected at 20 h in the GMN NPs-Cy5 group, but the intratumoral fluorescence was almost undetectable after 48 h. Considering the easily-aggregated properties of GMN NPs shown in Fig. 1, it was speculated that after injection the aggregated form of GMN NPs could slow down the erosion effect of interstitial fluid and prolong the retention time at tumors. However, after the injection of GME NPs, the intratumoral fluorescence intensity at 20 and 48 h was approximately 71.82% and 37.46% of that at 1 h, respectively. These results indicated that the addition of EGCG could also effectively form a "drug bank" at tumors, to maintain a longer intratumoral drug concentration and avoid systemic toxic side effects, but do not influence the degradation of GME NPs, in addition to the aforementioned improvement of nanoparticle stability and demethylation in tumor cells.

The PD-1/PD-L1 axis is a widely studied immune checkpoint. One of the mechanisms by which tumor cells in the TME escape the surveillance and killing of the immune system is to upregulate the expression of PD-L1[11,13]. And ICD inducers might upregulate the expression of PD-L1 by feedback[10,16,51]. As shown in Fig. 4C and Supporting Information Fig. S8, the expression of PD-L1 on the surface of tumor cells treated with different forms of GOx *in vitro* was upregulated. And the PD-L1 on tumor cells *in vivo* was all at a high expression level, but it was sharply decreased after intraperitoneal injection of αPD-L1 antibody. Therefore, GME NPs, combined with the PD-L1 antibody, might achieve a better anti-tumor immune effect.

Firstly, a single subcutaneous CT26 tumor model was established in BALB/c female mice[52,53]. When the volume of CT26 tumors reached about 75 mm^3, mice were randomly divided into six groups, named saline, GOx, αPD-L1, GMN NPs, GME NPs and GME NPs + αPD-L1. The dosing regimen was shown in Fig. 4D. According to the tumor volume curve, it could be seen that both GOx and αPD-L1 exhibited weak inhibition on the growth of CT26 tumors, and the TGI of GOx and αPD-L1 was less than 50% (Fig. 4E and F). After two administrations of GMN NPs and GME NPs, the tumor volume was well-suppressed before the 16th. It was a pity that from the 18th, the tumors re-entered the rapid growth stage (Fig. 4H). However, the survival of tumor-bearing mice treated with GME NPs was extended by 10 and 4 days, respectively, compared with the saline and GMN NPs groups (Fig. 4G). It was more satisfying that during the entire treatment, the tumor volume was well controlled in the GME NPs + αPD-L1 group, with a TGI of more than 95%. Moreover, the survival of mice in this combination group was significantly extended to 43.5 days, and there was no tumor recurrence observed in 2 of 10 tumor-bearing mice at the monitoring endpoint (180 days).

The excised tumors were fixed for sectioning and staining. Hematoxylin−eosin (H&E) staining showed that the tumors exhibited varying degrees of necrosis (Fig. 4I and Supporting Information Fig. S9). The necrosis area of the tumors in the GOx and αPD-L1 treatment groups was almost the same as that in the saline group, less than 10% of the total section area. Basically, consistent with the TGI data, the necrosis area of the tumors treated with GMN NPs, GME NPs, and GME NPs +αPD-L1 expanded rapidly, accounting for 33%, 50%, and 67% of the total area of the sections, respectively. Furthermore, in the GME NPs + αPD-L1 group, the proportion of apoptotic cells was the highest according to the TUNEL staining, and there were almost no Ki67 antigen-positive cells, suggesting that this combined therapy strategy had an excellent prognostic effect (Fig. S9).

In addition, the *in vivo* safety evaluation of the GME NPs was shown in Supporting Information Figs. S10 and S11D. Firstly, after different forms of GOx were intratumorally administered, there was no significant decrease in blood glucose, compared with the saline group, which might be due to the low dose of GOx administered in the efficacy experiment[19,44]. Secondly, during the efficacy experiment, the body weight of the treatment groups was also within the normal range. Finally, after the treatment, there were no abnormalities in blood cells represented by WBCs, blood biochemical indexes such as ALT and AST, and pathological section analysis of major organs. This once again indicated that this low-dose intratumoral administration was safe *in vivo*, with the induction of high-efficacy pyroptosis.

In order to further investigate the anti-tumor and anti-metastasis potential of GME NPs on other types of tumors, especially for immune "cold" tumors, the models of B16F10 subcutaneous malignant melanoma and 4T1 orthotopic breast cancer were established[54-58]. On the 8th day after B16F10 tumor implantation, the tumor volume reached approximately 80 mm^3, and treatments were carried out as planned (Supporting Information Fig. S11A). Obviously, the GME NPs + αPD-L1 group exhibited the best effects against the tumor with a TGI of 85.98%, followed by the GME NPs (67.35%) and GMN NPs group (35.42%), compared with the saline group (Fig. S11B, S11C, S11E and S11F). According to animal ethics, on the 16th and 18th days, mice in the saline and GMN NPs group basically reached the median of their lives, respectively (Fig. S11B, S11C and S11H). The median survival of mice in the GME NPs and GME NPs + αPD-L1 group was 21 and 24 days, respectively. Besides, H&E analysis of excised B16F10 tumors was carried out (Fig. S11G). In generally, the therapeutic effect on B16F10 tumors was not as ideal so to the CT26 model, which might be relevant to its malignancy and rapid growth. However, the tumor volume was

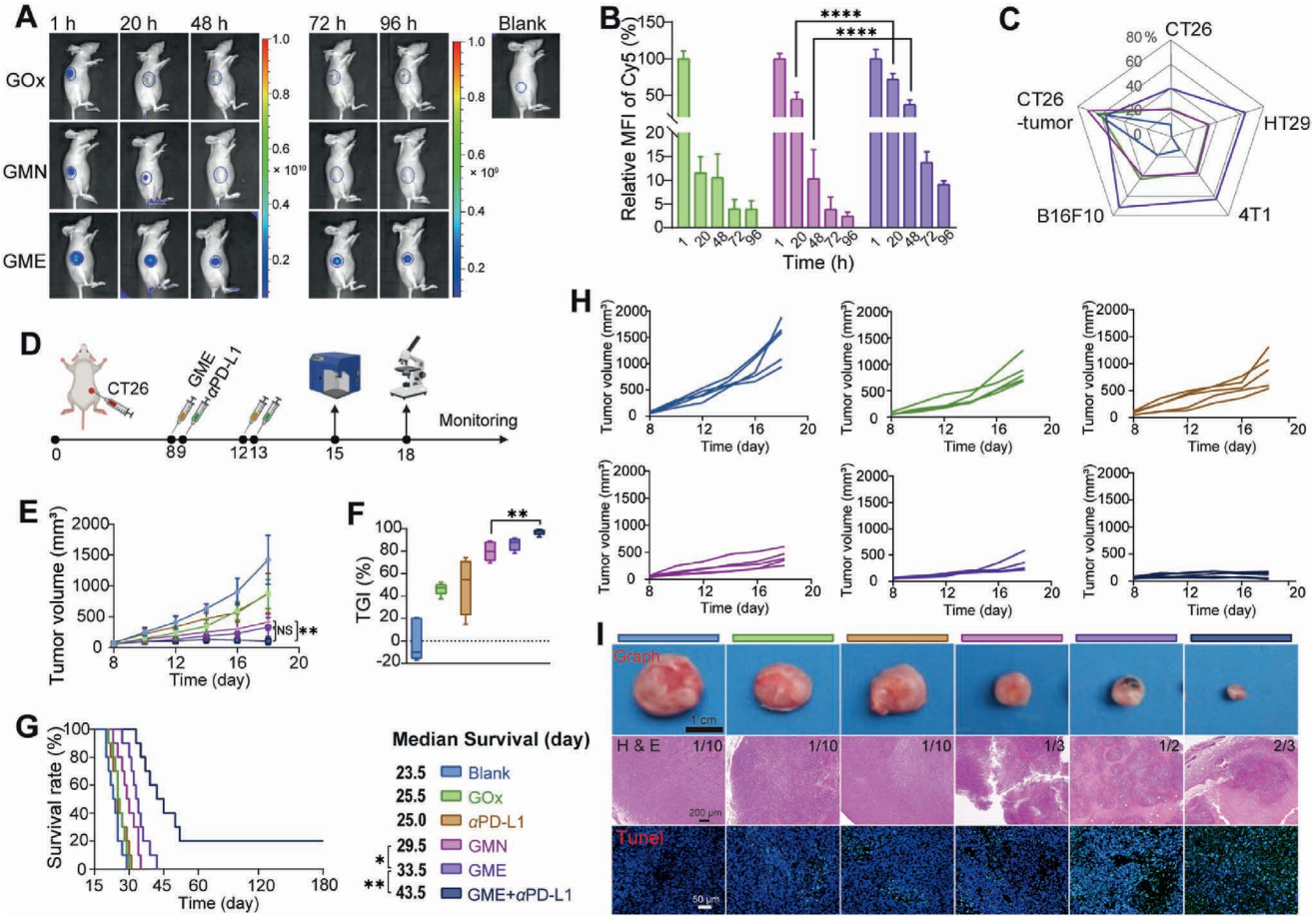

Figure 4 GME NPs exhibited an extended retention at CT26 tumors and excellent tumor growth inhibition combined with PD-L1 antibody. Representative *in vivo* fluorescent images of CT26 tumor-bearing mice (A) and semi-quantitative analysis of the Cy5 fluorescence intensity of the tumor sites (B) at 1, 20, 48, 72, and 96 h after administration ($n = 3$). (C) Proportion of positive PD-L1 cells in CT26, HT29, 4T1, B16F10 cells ($n = 3$), and CT26 tumors ($n = 4$) with different treatment. (D) Schematic diagram of dosing regimen. (E) The tumor volume growth ($n = 5$). (F) TGI evaluated on 18th day ($n = 5$). (G) Kaplan−Meier survival curves ($n = 10$). (H) Individual tumor volume curves ($n = 5$). (I) Representative graphs of tumors excised on 18th day (scale bar = 1 cm), staining images of H&E (scale bar = 200 μm) and TUNEL (scale bar = 50 μm). Statistical significance: ns, $P > 0.05$; *$P < 0.05$; **$P < 0.01$; ***$P < 0.001$; ****$P < 0.0001$.

effectively controlled during the period with the combination treatment, which was a hopeful sign. Therefore, it was reasonably speculated that GME NPs + αPD-L1 treatment might be able to achieve a better anti-tumor effect, by shortening the dosing interval or increasing the dosing frequency.

Meanwhile, the model of 4T1 orthotopic breast cancer was established, which was known for the immunosuppressive TME and ease of distant metastasis (Supporting Information Fig. S12). Significantly the tumor volume of the GME NPs + αPD-L1 group increased the slowest, followed by GME NPs, and it almost remained the same within 13 days (Fig. S12B and S12D). The relatively limited anti-tumor effects induced by GME NPs might be due to the hard texture of 4T1 tumors, and the unconducive distribution and release of drugs in tumors, as well as the shortage of the treatment period. However, it was obviously observed the differences in tumor inhibition between the GMN NPs and GME NPs group, which demonstrated again the superiority of dual-pathway induction of high efficiency pyroptosis for tumor therapy. In addition, the lungs of mice were excised on the 28th and 35th days to evaluate the inhibitory effects of different treatments on the distant spontaneous metastasis[58,59]. The weight of the lungs basically corresponded to the H&E analysis (Fig. S12E−S12G). On the 28th day, a few tumor metastases were obviously observed in the lungs of the saline group, and metastases were occasionally found in that of the GMN NPs group. On the 35th day, the original morphology of the lungs from the saline group was almost invisible, instead of metastatic tumors. And a large number of metastases were also shown in the GMN NPs group. However, there were nearly no metastases found in the GME NPs and GME NPs + αPD-L1 group, but the lungs also showed slight edema on the 35th day. GME NPs and GME NPs + αPD-L1 group both exhibited similar and remarkable inhibitory effects on tumor metastasis to lungs, further strongly demonstrating the superiority of the GME NPs. And there might be several reasons why no obvious lung metastases were found in mice treated with GME NPs. On the one hand, GME-induced immunostimulation effects might reshape the immune microenvironment, which is unfavorable for tumor cells colonization at distant sites. On the other hand, EGCG presented on the GME NPs could also adhere to tumor cells to prevent them from migrating from the tumor site into the blood and then colonizing in distant tissues.

3.4. *GME NPs induced efficient pyroptosis in tumors which triggered a potent anti-tumor immune response*

Furthermore, the preliminary study on the mechanism of the anti-tumor effects of the GME NPs and the combination with αPD-L1 antibody was conducted (Fig. 5A). Consistent with the *in vitro* results, tumors with GME NPs treatment exposed more CRT and secreted more HMGB1 than other treatment (Fig. 5B and Fig. S9D and S9E), suggesting that potent ICD effects caused by GME NPs treatment might contribute to the recruitment and activation of

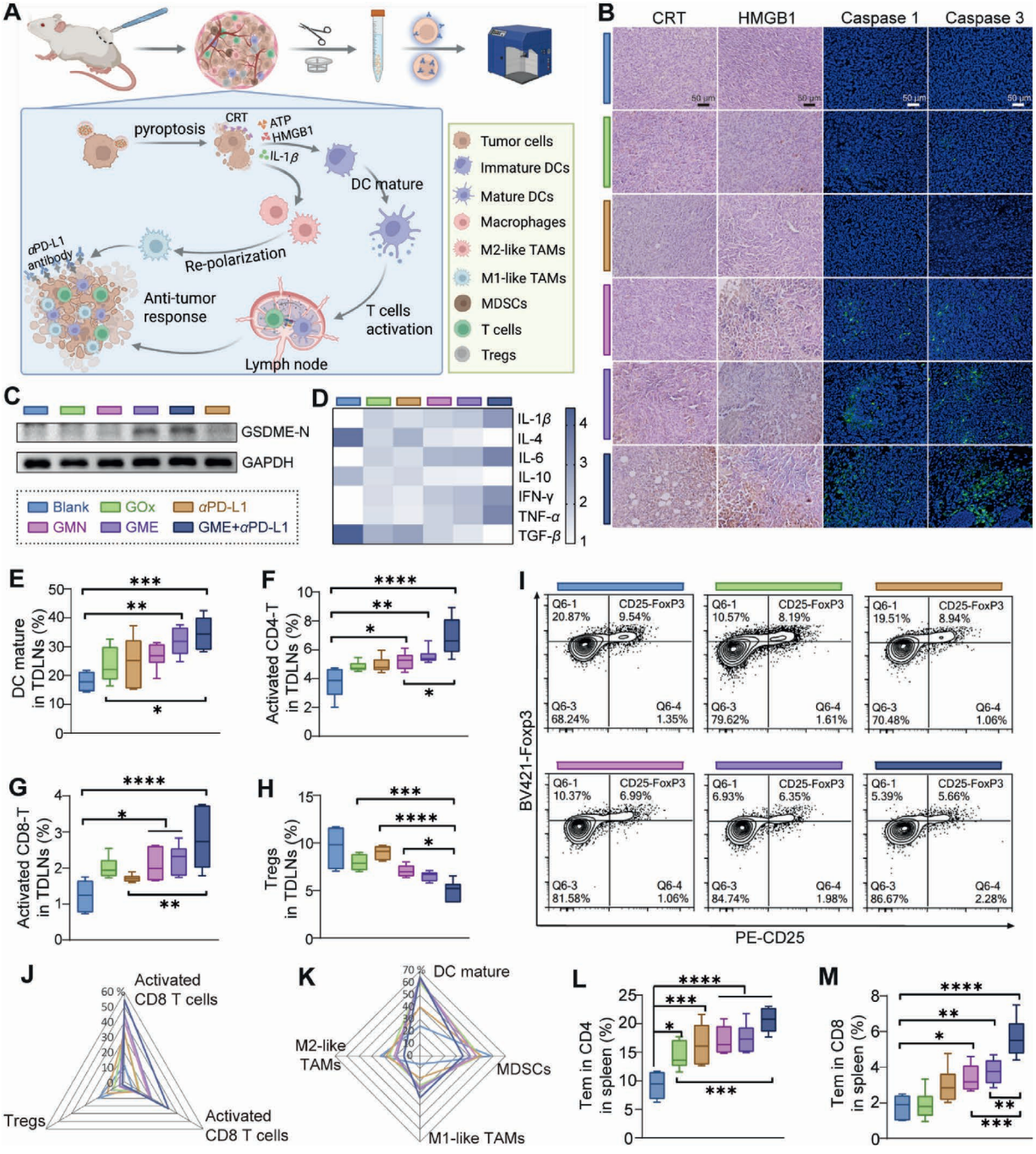

Figure 5 GME NPs combined with αPD-L1 antibody induced efficient pyroptosis and then triggered a potent anti-tumor immune response *in vivo*. (A) Flowchart of the preparation and staining of single-cell suspension of tumors, and the schematic diagram of the *in vivo* anti-tumor mechanism of GME NPs. (B) IHC or IF analysis of CRT, HMGB1, cleaved caspase 1, and cleaved caspase 3 in tumor sections. Scale bar = 50 μm. (C) WB analysis of GSDME-full length and GSDME-N terminal in tumors. (D) Heat map of the cytokines in tumors characterized by ELISA. Proportion of mature DCs (E), activated CD4 T cells (F), activated CD8 T cells (G), and Tregs (H) in TDLNs. (I) Representative flow cytometry images of Tregs in TDLNs. (J) Radar map of the proportion of activated CD4 T cells, activated CD8 T cells, and Tregs in tumors. (K) Radar map of the proportion of mature DCs, M1-like TAMs, M2-like TAMs, and MDSCs in tumors. Proportion of Tef in CD4 T cells (L) and Tef in CD8 T cells (M) in spleens. Data are shown as mean ± SD ($n = 5$). Statistical significance: ns, $P > 0.05$; *$P < 0.05$; **$P < 0.01$; ***$P < 0.001$; ****$P < 0.0001$.

immune cells and stimulate anti-tumor immune responses. Furthermore, high expression levels of cleaved caspase 1 were observed in the tumors treated with GMN NPs and GME NPs, both of which were much higher than those in the GOx group (Fig. 5B and Fig. S9F), which might be relevant to the result that free GOx was quickly carried away by the interstitial fluid after intratumoral injection. In addition, significantly higher expression levels of cleaved caspase 3 and GSDME-N terminal were also observed in the GME NPs group (Fig. 5B and C and Supporting Information Fig. S13A). These results indicated that EGCG released from the GME NPs could also restore the expression of GSMDE *in vivo*, and cleaved by active caspase 3 to enhance pyroptosis for better anti-tumor effects.

Inspired by the potent immune response stimulated by pyroptosis, immune cells and cytokines in tumors were quantitatively estimated[1,18,39,60]. First of all, after treatment with the GME NPs, the secretion levels of anti-tumor cytokines represented by IL-1β, IL-6, IFN-γ, and TNF-α were significantly increased, while the levels of pro-tumor cytokines represented by IL-4, IL-10, and TGF-β were decreased (Fig. 5D and Fig. S13B−S13H). Moreover, the trends of these data were further enhanced in tumors after treatment with GME NPs + αPD-L1 antibody. Meanwhile, tumor-draining lymph nodes (TDLNs), spleens, and tumors were collected to prepare the single-cell suspensions for analysis of immune cells[46,47,54]. The maturation of DCs is one of the prerequisites for inducing anti-tumor immune responses[61-63]. The proportion of mature DCs in the GME NPs + αPD-L1 group was 1.93 times that of the saline group in TDLNs and 1.88 times that in tumors (Fig. 4E−K and Supporting Information Figs. S14A, S14B and S15). Subsequently, mature DCs initiate anti-tumor immune responses by recruiting and activating T cells[63-65]. Obviously, whether in TDLNs or in tumors, the highest proportion of activated CD4 T cells and CD8 T cells, and the lowest proportion of the immunosuppressive regulatory T cells (Tregs) were observed in the GME NPs + αPD-L1 group, followed by GME NPs (Fig. 5F−J and Supporting Information Figs. S14C−S14G and S16). In other words, a large quantity of CD4 T cells and CD8 T cells were recruited into the tumor and massively activated after the combination treatment. At the proportion of Tregs decreased from 19.92% in the saline group to 2.58%, suggesting that the immunosuppressive microenvironment was greatly alleviated. In addition, M1-like tumor-associated macrophages (TAMs), regarded as a type of immune-activated cells, exhibited varying degrees of upregulation after treatments with different forms of GOx. The proportion of M1-TAMs in the GME NPs + αPD-L1 group was as high as 5.17 times that of the saline group (Fig. 5K and Supporting Information Figs. S14H and S17). Meanwhile, M2-like TAMs and MDSCs, known as immunosuppressive cells with pro-tumor effects, had the lowest abundance in the GME NPs + αPD-L1 group, which were only 40.50% and 61.38% of that in the saline group, respectively (Fig. 5K and Figs. S14I, S14J and S17). Finally, the effector T cells (Tef) gated in CD4 T cells and in CD8 T cells was 2.61 times and 3.68 times that of the saline group, respectively (Fig. 5L−M and Supporting Information Fig. S18), which might be the reasons why in the two models of CT26 tumors, the tumor-bearing mice in the GME NPs + αPD-L1 group exhibited tumor regression at varying degrees.

In general, GME NPs combined with αPD-L1 antibody, through the simultaneous activation of caspase 1-GSDMD and caspase 3-GSDME-mediated pyroptosis signals, could not only induce powerful ICD effects, but also further stimulate the activation of immune cells and reshape the immunosuppressive TME, achieving a potent and lasting effect against tumors.

3.5. GME NPs combined with αPD-L1 antibody exhibited a potent immune memory effect on CT26 re-challenge model

Considering the excellent tumor inhibition effect and the potential immune memory effects of the combined therapy, CT26 cells were inoculated on the other side of the back of CT26

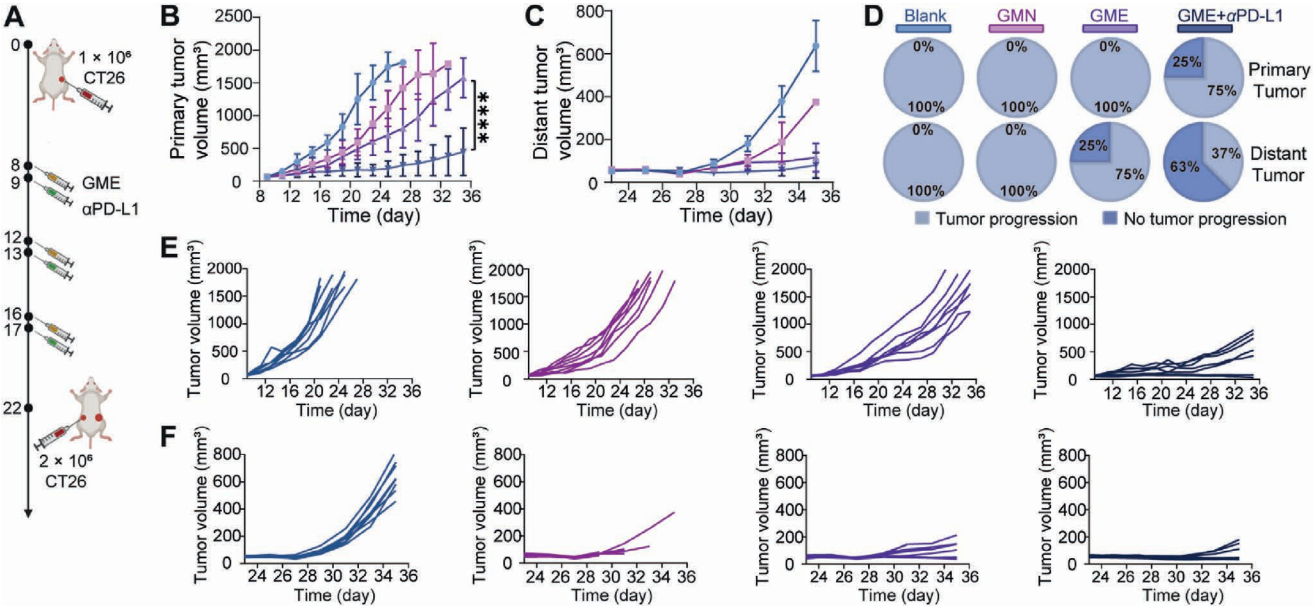

Figure 6 GME NPs combined with αPD-L1 antibody exhibited a potent immune memory effect on CT26 re-challenge model. (A) Schematic diagram of dosing regimen. Tumor volume growth of the primary tumor (B) and distant tumor (C). (D) Rate of mice without CT26 tumor progression. Individual tumor volume curves of the primary tumor (E) and distant tumor (F). Data are shown as mean ± SD (n = 8). Statistical significance: ns, $P > 0.05$; *$P < 0.05$; **$P < 0.01$; ***$P < 0.001$; ****$P < 0.0001$.

tumor-bearing mice to evaluate the inhibitory effect on distant tumors of the immune response stimulated by the combination therapy[46,47]. The experimental design and dosing regimen were shown in Fig. 6A. The changes in volume of the primary tumors were basically consistent with the aforementioned unilateral CT26 model (Fig. 6B and E). However, after a short period of colonization, the distant tumors in different treatment groups exhibited varied growth rates (Fig. 6C and F). During the monitoring process, several mice in the GMN NPs treatment group were sacrificed because the primary tumors exceeded the requirements of animal ethics. And on the 33rd day, there were only 2 of the tumor-bearing mice still alive in the GMN NPs group, and the distant tumor volumes of them were 254.63 and 123.41 mm^3, respectively. On the 35th day, there were six of the tumor-bearing mice alive in the GME NPs group, and the distant tumors showed signs of regression in 2 of the tumor-bearing mice (Fig. 6D). It was worth emphasizing that the distant tumors in the GME NPs + αPD-L1 group not only showed an extremely slow growth rate, but also 5/8 of them showed tumor regression. And there were no signs of tumor recurrence until 50 days. This suggested that the combination strategy not only had a superior tumor inhibition effect but also could stimulate a strong immune response to inhibit homologous distant tumors or tumor recurrence.

4. Conclusions

In this study, the biomineralized-like nanoparticles named GME NPs were constructed by a one-pot approach to chelate GOx and EGCG in the basic framework composed of Mn^{2+} and imidazole, which effectively addressed the challenge of the simultaneous loading and intracellular delivery of a hydrophilic small-molecule epigenetic modulator (EGCG) and a large enzyme protein (GOx, ~150 kDa) in one particle. And it was additionally found that EGCG served two mechanistically relevant roles simultaneously beyond "packaging". On the one hand, it acted as a structural component stabilizing the nanoparticle framework, significantly improving the stability of Mn-based MOF/MPN hybrids. On the other hand, it also functioned as a functional epigenetic regulator, restoring GSDME expression *via* demethylation. The dual structural−functional role of EGCG within one nanoparticle is, to our knowledge, previously unreported. Moreover, GME NPs could maintain the enzymatic activity of encapsulated GOx over 90% for at least 2 weeks, and extended the retention of GME NPs at CT26 tumors after intratumoral administration due to the adhesion effects.

This study validated the demethylation effect of EGCG on the DFNA5 gene at the gene level, as well as the increased the expression of GSDME at the transcription and translation levels. Subsequently, inspired by the anti-tumor efficacy of pyroptosis, GOx was used as the "initiator" to activate pyroptosis mediated by the caspase 1-GSDMD pathway through the consumption of intratumoral glucose, accompanied by the activation of caspase 3. Concurrently, EGCG functioned as "accelerants" that converted apoptosis into pyroptosis *via* GSDME, which was upregulated and subsequently cleaved by active caspase 3. Due to the potent effects of GME NPs against tumors, this dual-pathway activation of the pyroptosis strategy required the GOx at a low concentration, nearly without toxicity *in vivo*. In addition, it was found that different forms of GOx could upregulate the expression of PD-L1 on the surface of tumor cells while inducing pyroptosis, which might restore the sensitivity of tumors to ICIs. Therefore, GME NPs were subsequently combined with αPD-L1 antibody *in vivo*, and outstanding inhibitory effects were achieved in several types of "cold" tumor models, such as CT26, B16F10, and 4T1 tumors. Among them, 2 of 10 tumor-bearing mice were cured in the CT26 single tumor model, and 5 of 8 tumor-bearing mice showed no signs of distant tumor recurrence in the CT26 re-challenge tumor model, indicating that the combined treatment triggered an effective immune effect *in vivo*. Moreover, GME NPs achieved more than 85% of TGI in B16F10 tumor model, and the metastasis to lungs was also effectively inhibited in the 4T1 tumor model. In general, our design ensured intracellular delivery of GOx and EGCG, restored GSDME to rewire caspase-3 signaling from apoptosis to pyroptosis, and activated both GSDMD and GSDME pathways in the same cell, thereby amplifying ICD effects while avoiding the immunosuppressive consequences of apoptosis.

It was worth mentioning that not only in CT26, but also the high sensitivity and response rate of human colon cancer cells named HT29 to dual-pathway pyroptosis-activating nanoparticles named GME NPs *in vitro* were verified, which might be due to the high methylation in HT29. However, except for HT29, DNA methylation, always accompanied by the rare expression of GSDME, is a common phenomenon in many types of human tumor cells according to the literature research[4,24]. Therefore, GME NPs might bring a new prospect for the research and therapy of cancer in the clinic. Besides, this study mainly focused on proposing and realizing the therapeutic effect of the dual-pathway pyroptosis-activating strategy through pharmaceutics methods. Then, how to improve its blood circulation and tumor targeting for intravenous administration to meet the requirements of other types of tumor models is our next direction of consideration and exploration.

Acknowledgments

This work was financially supported by National Key R&D Program of China (2024YFA1210100) and National Natural Science Foundation of China (82373799). The schematic diagrams in this article were created in BioRender. Feng S. (2026) https://BioRender.com/800102fAuthor contributions.

Author contributions

Tao Gong and Jiaxing Feng conceived and planned the study. Jiaxing Feng carried out the experiments, generated and analyzed data, and wrote the original manuscript. Kun Xiong, Yuan Xue, Yating Wang, and Xiuhua Wu helped with *in vitro* and *in vivo* studies. Qing Lin, Xun Sun, Huile Gao, Zhirong Zhang and Tao Gong helped with manuscript editing.

Conflicts of interest

The authors declare no conflicts of interest.

Appendix A. Supporting information

Supporting information to this article can be found online at https://doi.org/10.1016/j.apsb.2026.01.034.

References

1. Broz P, Pelegrín P, Shao F. The gasdermins, a protein family executing cell death and inflammation. *Nat Rev Immunol* 2020;**20**:143−57.
2. Lu LQ, Zhang Y, Tan XM, Merkher Y, Leonov S, Zhu L, et al. Emerging mechanisms of pyroptosis and its therapeutic strategy in cancer. *Cell Death Discov* 2022;**8**:338.
3. Shi JJ, Zhao Y, Wang K, Shi XY, Wang Y, Huang HW, et al. Cleavage of GSDMD by inflammatory caspases determines pyroptotic cell death. *Nature* 2015;**526**:660−5.
4. Wang YP, Gao WQ, Shi XY, Ding JJ, Liu W, He HB, et al. Chemotherapy drugs induce pyroptosis through caspase-3 cleavage of a gasdermin. *Nature* 2017;**547**:99.
5. Yu P, Zhang X, Liu N, Tang L, Peng C, Chen X. Pyroptosis: mechanisms and diseases. *Signal Transduct Targeted Ther* 2021;**6**:128.
6. Liu X, Xia SY, Zhang ZB, Wu H, Lieberman J. Channelling inflammation: gasdermins in physiology and disease. *Nat Rev Drug Discov* 2021;**20**:384−405.
7. Chen DS, Mellman I. Oncology meets immunology: the cancer-immunity cycle. *Immunity* 2013;**39**:1−10.
8. Galluzzi L, Buqué A, Kepp O, Zitvogel L, Kroemer G. Immunogenic cell death in cancer and infectious disease. *Nat Rev Immunol* 2017;**17**: 97−111.
9. Galluzzi L, Buqué A, Kepp O, Zitvogel L, Kroemer G. Immunological effects of conventional chemotherapy and targeted anticancer agents. *Cancer Cell* 2015;**28**:690−714.
10. Song WT, Shen LM, Wang Y, Liu Q, Goodwin TJ, Li JJ, et al. Synergistic and low adverse effect cancer immunotherapy by immunogenic chemotherapy and locally expressed PD-L1 trap. *Nat Commun* 2018;**9**:2237.
11. Yi M, Niu MK, Xu LP, Luo SX, Wu KM. Regulation of PD-L1 expression in the tumor microenvironment. *J Hematol Oncol* 2021;**14**:10.
12. Chang CH, Qiu J, O'Sullivan D, Buck MD, Noguchi T, Curtis JD, et al. Metabolic competition in the tumor microenvironment is a driver of cancer progression. *Cell* 2015;**162**:1229−41.
13. Escors D, Gato-Cañas M, Zuazo M, Arasanz H, García-Granda MJ, Vera R, et al. The intracellular signalosome of PD-L1 in cancer cells. *Signal Transduct Targeted Ther* 2018;**3**:26.
14. Hu YX, Liu Y, Zong LJ, Zhang WY, Liu RZ, Xing QC, et al. The multifaceted roles of GSDME-mediated pyroptosis in cancer: therapeutic strategies and persisting obstacles. *Cell Death Dis* 2023;**14**:836.
15. Zhang ZB, Zhang Y, Xia SY, Kong Q, Li SY, Liu X, et al. Gasdermin E suppresses tumour growth by activating anti-tumour immunity. *Nature* 2020;**579**:415.
16. Qiu NS, Liu Y, Liu Q, Chen YZ, Shen LM, Hu MY, et al. Celastrol nanoemulsion induces immunogenicity and downregulates PD-L1 to boost abscopal effect in melanoma therapy. *Biomaterials* 2021;**269**: 120604.
17. Yang F, Bettadapura SN, Smeltzer MS, Zhu H, Wang SZ. Pyroptosis and pyroptosis-inducing cancer drugs. *Acta Pharmacol Sin* 2022;**43**: 2462−73.
18. Li JJ, Anraku Y, Kataoka K. Self-boosting catalytic nanoreactors integrated with triggerable crosslinking membrane networks for initiation of immunogenic cell death by pyroptosis. *Angew Chem Int Ed* 2020;**59**:13526−30.
19. Zhang SJ, Zhang Y, Feng YJ, Wu JY, Hu YY, Lin L, et al. Biomineralized two-enzyme nanoparticles regulate tumor glycometabolism inducing tumor cell pyroptosis and robust antitumor immunotherapy. *Adv Mater* 2022;**34**:2206851.
20. Rubinfeld B, Upadhyay A, Clark SL, Fong SE, Smith V, Koeppen H, et al. Identification and immunotherapeutic targeting of antigens induced by chemotherapy. *Nat Biotechnol* 2006;**24**:205−9.
21. Wang YJ, Fletcher R, Yu J, Zhang L. Immunogenic effects of chemotherapy-induced tumor cell death. *Genes Dis* 2018;**5**:194−203.
22. Wei YT, Wang XR, Yan CG, Huang F, Zhang YP, Liu XM, et al. Thymosin a-1 reverses M2 polarization of tumor-associated macrophages during efferocytosis. *Cancer Res* 2022;**82**:1991−2002.
23. Jiang MX, Qi L, Li LS, Li YJ. The caspase-3/GSDME signal pathway as a switch between apoptosis and pyroptosis in cancer. *Cell Death Discov* 2020;**6**:112.
24. Rogers C, Fernandes-Alnemri T, Mayes L, Alnemri D, Cingolani G, Alnemri ES. Cleavage of DFNA5 by caspase-3 during apoptosis mediates progression to secondary necrotic/pyroptotic cell death. *Nat Commun* 2017;**8**:14128.
25. Akino K, Toyota M, Suzuki H, Imai T, Maruyama R, Kusano M, et al. Identification of as a target of epigenetic inactivation in gastric cancer. *Cancer Sci* 2007;**98**:88−95.
26. Kim MS, Chang X, Yamashita K, Nagpal JK, Baek JH, Wu G, et al. Aberrant promoter methylation and tumor suppressive activity of the gene in colorectal carcinoma. *Oncogene* 2008;**27**:3624−34.
27. Shan LL, Gao GZ, Wang WW, Tang W, Wang ZT, Yang Z, et al. Self-assembled green tea polyphenol-based coordination nanomaterials to improve chemotherapy efficacy by inhibition of carbonyl reductase 1. *Biomaterials* 2019;**210**:62−9.
28. Fang MZ, Wang YM, Ai N, Hou Z, Sun Y, Lu H, et al. Tea polyphenol (−)-epigallocatechin-3-gallate inhibits DNA methyltransferase and reactivates methylation-silenced genes in cancer cell lines. *Cancer Res* 2003;**63**:7563−70.
29. Agarwal A, Kansal V, Farooqi H, Prasad R, Singh VK. Epigallocatechin gallate (EGCG), an active phenolic compound of green tea, inhibits tumor growth of head and neck cancer cells by targeting DNA hypermethylation. *Biomedicines* 2023;**11**:789.
30. Lv XJ, Huang J, Min J, Wang HR, Xu YY, Zhang ZM, et al. Multi-signaling pathway activation by pH responsive manganese particles for enhanced vaccination. *J Control Release* 2023;**357**:109−19.
31. Wang RF, Qiu MS, Zhang L, Sui MJ, Xiao L, Yu Q, et al. Augmenting immunotherapy *via* bioinspired MOF-based ROS homeostasis disruptor with nanozyme-cascade reaction. *Adv Mater* 2023;**35**: 202306748.
32. Guo CQ, Wu MY, Guo ZF, Zhang RP, Wang ZJ, Peng X, et al. Hypoxia-responsive golgi-targeted prodrug assembled with anthracycline for improved antitumor and antimetastasis efficacy. *ACS Nano* 2023;**17**:24972−87.
33. Xu WJ, Lin ZX, Pan SJ, Chen JQ, Wang TZ, Cortez-Jugo C, et al. Direct assembly of metal-phenolic network nanoparticles for biomedical applications. *Angew Chem Int Ed* 2023;**62**:202312925.
34. Kumar P, Bansal V, Paul AK, Bharadwaj LM, Deep A, Kim KH. Biological applications of zinc imidazole framework through protein encapsulation. *Appl Nanosci* 2016;**6**:951−7.
35. Kaur H, Mohanta GC, Gupta V, Kukkar D, Tyagi S. Synthesis and characterization of ZIF-8 nanoparticles for controlled release of 6-mercaptopurine drug. *J Drug Deliv Sci Technol* 2017;**41**:106−12.
36. Wang C, Sudlow G, Wang Z, Cao S, Jiang Q, Neiner A, et al. Metal-organic framework encapsulation preserves the bioactivity of protein therapeutics. *Adv Healthcare Mater* 2018;**7**:e1800950.
37. Chakrabarti P. Interaction of metal-ions with carboxylic and carboxamide groups in protein structures. *Protein Eng* 1990;**4**:49−56.
38. Xu QD, Yu ZL, He Q, Zeng WC. Controllable supramolecular self-assembly of proteins mediated by metal-polyphenols: characteristics and their applications on encapsulating hydrophobic small molecules. *Chem Eng J* 2025;**505**:159881.
39. Fan JX, Deng RH, Wang H, Liu XH, Wang XN, Qin R, et al. Epigenetics-based tumor cells pyroptosis for enhancing the immunological effect of chemotherapeutic nanocarriers. *Nano Lett* 2019;**19**: 8049−58.
40. Ferrari E, Bettuzzi S, Naponelli V. The potential of epigallocatechin gallate (EGCG) in targeting autophagy for cancer treatment: a narrative review. *Int J Mol Sci* 2022;**23**:6075.
41. Marín V, Burgos V, Pérez R, Maria DA, Pardi P, Paz C. The potential role of epigallocatechin-3-gallate (EGCG) in breast cancer treatment. *Int J Mol Sci* 2023;**24**:10737.
42. Brumatti G, Sheridan C, Martin SJ. Expression and purification of recombinant annexin V for the detection of membrane alterations on apoptotic cells. *Methods* 2008;**44**:235−40.

43. Deng YD, Jia FY, Jiang PH, Chen LQ, Xing LY, Shen XR, et al. Biomimetic nanoparticle synchronizing pyroptosis induction and mitophagy inhibition for anti-tumor therapy. *Biomaterials* 2023;**301**: 122293.
44. Ding BB, Zheng P, Tan J, Chen H, Bian YL, Yang CZ, et al. Pyroptosis adjuvants: gram-scale production, cascade catalysis, and *in situ* antitumor immunity activation. *Chem Mater* 2022;**34**:1800−8.
45. Chen BL, Yan Y, Yang Y, Cao G, Wang X, Wang YQ, et al. A pyroptosis nanotuner for cancer therapy. *Nat Nanotechnol* 2022;**17**: 788.
46. Zhao X, Zhao RF, Nie GJ. Nanocarriers based on bacterial membrane materials for cancer vaccine delivery. *Nat Protoc* 2022;**17**:2240−74.
47. Tan MX, Cao GL, Wang RP, Cheng L, Huang WP, Yin Y, et al. Metal-ion-chelating phenylalanine nanostructures reverse immune dysfunction and sensitize breast tumour to immune checkpoint blockade. *Nat Nanotechnol* 2024;**19**:1903−13.
48. De Henau O, Rausch M, Winkler D, Campesato LF, Liu CL, Hirschhorn-Cymerman D, et al. Overcoming resistance to checkpoint blockade therapy by targeting PI3Kγ in myeloid cells. *Nature* 2016; **539**:443−7.
49. Song YD, Bugada L, Li RT, Hu HX, Zhang LC, Li CY, et al. Albumin nanoparticle containing a PI3Kγ inhibitor and paclitaxel in combination with α-PD1 induces tumor remission of breast cancer in mice. *Sci Transl Med* 2022;**14**:3649.
50. Chen ZJ, Farag MA, Zhong ZF, Zhang C, Yang Y, Wang SP, et al. Multifaceted role of phyto-derived polyphenols in nanodrug delivery systems. *Adv Drug Deliv Rev* 2021;**176**:113870.
51. Kroemer G, Galluzzi L, Kepp O, Zitvogel L. Immunogenic cell death in cancer therapy. *Annu Rev Immunol* 2013;**31**:51−72.
52. Li XL, Duan ZY, Chen XT, Pan DY, Luo Q, Gu L, et al. Impairing tumor metabolic plasticity *via* a stable metal-phenolic-based polymeric nanomedicine to suppress colorectal cancer. *Adv Mater* 2023; **35**:2300548.
53. Zhen WY, Liu Y, An SJ, Jiang XE. Glutathione-induced *in situ* michael addition between nanoparticles for pyroptosis and immunotherapy. *Angew Chem Int Ed* 2023;**62**:e202301866.
54. Feng JX, Xiang L, Fang CL, Tan YL, Li Y, Gong T, et al. Dual-targeting of tumor cells and tumor-associated macrophages by palmitic acid modified albumin nanoparticles for antitumor and antimetastasis therapy. *Acs Appl Mater Inter* 2022;**14**:14887−902.
55. Chen WF, Song YS, Bai ST, He CT, Guo ZF, Zhu YN, et al. Cloaking mesoporous polydopamine with bacterial membrane vesicles to amplify local and systemic antitumor immunity. *ACS Nano* 2023;**17**: 7733−49.
56. Galon J, Bruni D. Approaches to treat immune hot, altered and cold tumours with combination immunotherapies. *Nat Rev Drug Discov* 2019;**18**:197−218.
57. Spranger S, Bao RY, Gajewski TF. Melanoma-intrinsic β-catenin signalling prevents anti-tumour immunity. *Nature* 2015;**523**. 231-U61.
58. McGinnis CS, Miao Z, Superville D, Yao WN, Goga A, Reticker-Flynn NE, et al. The temporal progression of lung immune remodeling during breast cancer metastasis. *Cancer Cell* 2024;**42**:1018−31.
59. Fares J, Fares MY, Khachfe HH, Salhab HA, Fares Y. Molecular principles of metastasis: a hallmark of cancer revisited. *Signal Transduct Tar* 2020;**5**:28.
60. Tang R, Xu J, Zhang B, Liu J, Liang C, Hua J, et al. Ferroptosis, necroptosis, and pyroptosis in anticancer immunity. *J Hematol Oncol* 2020;**13**:110.
61. Chen J, Duan YH, Che JY, Zhu JW. Dysfunction of dendritic cells in tumor microenvironment and immunotherapy. *Cancer Commun* 2024; **44**:1047−70.
62. Wang YY, Xiang Y, Xin WX, Wang XW, Peng XC, Liu XQ, et al. Dendritic cell biology and its role in tumor immunotherapy. *J Hematol Oncol* 2020;**13**:107.
63. Iwasaki A, Medzhitov R. Control of adaptive immunity by the innate immune system. *Nat Immunol* 2015;**16**:343−53.
64. Hammerich L, Davis TA, Keler T, Salazar AM, Brody J. Combining vaccination with immune checkpoint blockade induces long-term regression of lymphoma tumors. *Blood* 2016;**128**:465.
65. Pittet MJ, Di Pilato M, Garris C, Mempel TR. Review dendritic cells as shepherds of T cell immunity in cancer. *Immunity* 2023;**56**: 2218−30.